

The 2017 M_w 6.6 Poso Earthquake: Implications for Extrusion Tectonics in Central Sulawesi

by Shuai Wang, Caijun Xu, Wenbin Xu, Zhi Yin, Yangmao Wen, and Guoyan Jiang

ABSTRACT

Determining how faults behave during large earthquakes can help provide insight into the mechanism of regional tectonism. Here, we use Advanced Land Observing Satellite-2 (ALOS-2) and Sentinel-1 Interferometric Synthetic Aperture Radar (InSAR) data to estimate the source parameters of the 2017 M_w 6.6 Poso earthquake, eastern Indonesia. The results show that the coseismic rupture was predominated by normal faulting at depths of 3–10 km, whereas some distinct dextral strike slip is also resolved along the down-dip direction of normal-faulting zones. We analyze the background seismicity, regional topography, and fault kinematics to investigate the present-day tectonics of central Sulawesi as well as its evolutionary processes. Our preferred slip model provides support for the proposed kinematic model that attributes the extension in central Sulawesi to gravitational collapse, in which mass lateral extrusion along the large-scale Palu-Koro strike-slip fault played an important role.

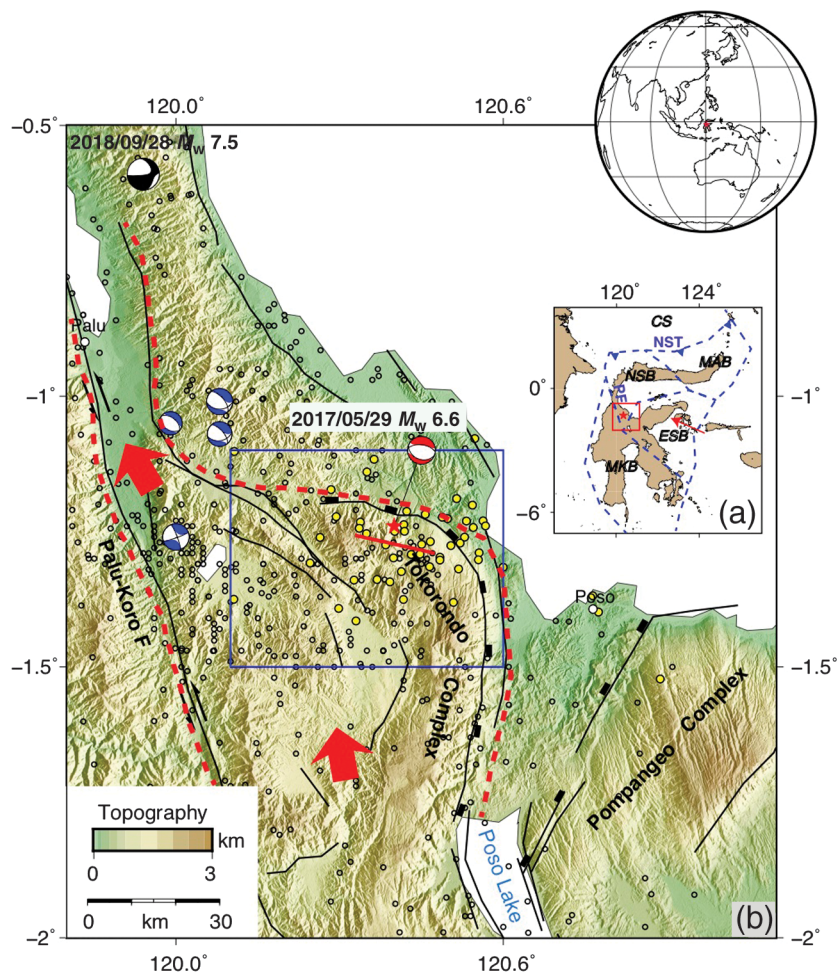
Electronic Supplement: Table of Synthetic Aperture Radar (SAR) data used in this study, and figures showing decomposed vertical displacement from ascending and descending ALOS-2 SAR data, uncertainty analysis of the source parameters, trade-off curve between slip roughness and weighted misfit of data, uncertainty of the inverted distributed slip model, and checkerboard test of slip inversion of 2017 Poso earthquake.

INTRODUCTION

The K-shaped island of Sulawesi (Fig. 1a) developed as a complex tectonic unit in eastern Indonesia in response to Cretaceous and Cenozoic accretion by accommodating the convergence among three tectonic plates in that region (i.e., the Australian, Eurasian, and Pacific plates; Hamilton, 1979). Some kinematic explanations, such as a model involving elastic, rotating microblocks (e.g., Socquet *et al.*, 2006), have been proposed to investigate the tectonic movements in Sulawesi, in spite of the ongoing controversy regarding the number of mi-

croblocks (Cummins and Meilano, 2017). Sulawesi has experienced numerous different $M \geq 6$ earthquakes, especially along the boundaries of the aforementioned microblocks, indicating that this region is undergoing complex tectonic processes involving collision (Silver *et al.*, 1983; Hall and Spakman, 2015) and transtension (Bellier *et al.*, 2006).

As an active part of Sulawesi, central Sulawesi was produced from the multistage subduction and collision of the tectonic plates (Bellier *et al.*, 2006). It is bifurcated by the large-scale northwest-trending Palu-Koro fault and divided into two parts: western central Sulawesi (northern part of the MKB, shown in Fig. 1a) and eastern central Sulawesi (hereafter ECS, shown in Fig. 1b). Western central Sulawesi presently moves as a rigid block that features a low level of seismicity (e.g., Stevens *et al.*, 1999). In contrast, ECS presents significant northeast–southwest-oriented extension, as revealed by Global Positioning System (GPS) measurements (Socquet *et al.*, 2006; Sarsito *et al.*, 2017) and geomorphic investigations (Spencer, 2010, 2011). This activity is consistent with focal mechanisms of local earthquakes (Fig. 1b); four $M_w \geq 5.5$ normal-faulting earthquakes with nodal planes oriented northwest–southeast occurred within ECS. These normal-faulting earthquakes are the most obvious embodiment of the active northeast–southwest extension of ECS. Although it is widely accepted that extensional tectonic settings provide an environment for the formation of normal faults, explanations for the driving force of extension differ significantly. For instance, Molnar and Tapponnier (1978) proposed that the east–west extension in Tibetan plateau (hereafter, TP) may have directly resulted from gravitational collapse, whereas others (e.g., Copley *et al.*, 2011) treated such extension in TP as a result of strike-slip faulting. Elliott *et al.* (2010) examined the relation between moment release of normal-faulting earthquakes and surface heights that highlights the strong dependence of extensional faulting on gravitational potential energy. Accordingly, mechanisms that are responsible for the extension in ECS remain largely unknown. Hence, the determination of how normal faults behave



▲ Figure 1. (a) Kinematic block model of Sulawesi (Socquet *et al.*, 2006) with the block boundaries depicted by blue dashed lines. The red arrow represents the direction of collision between the Banggai-Sula block and the eastern arm of Sulawesi. The red rectangle outlines the bounds of panel (b). (b) Tectonic background of the 2017 Poso earthquake. The focal mechanism plots represent the Global Centroid Moment Tensor (CMT) of the 2017 Poso earthquake (red), the $M_w \geq 5.5$ historical earthquakes (blue), and the 2018 Palu $M_w 7.5$ earthquake (black). Yellow dots represent the aftershocks recorded by the International Seismological Centre (ISC). Black circles represent the ISC $M > 2$ historical background seismicity, absent those that occurred within one month after the $M_w \geq 5.5$ earthquakes. Black lines denote the regional faults. The red line shows the up-dip projection of the fault plane determined through uniform slip modeling. Red dashed lines depict the model of a funnel-shaped structure we propose in this study. Thick red arrows indicate the southern inlet and northern outlet of the funnel-shaped structure. The blue rectangle outlines the coverage of the synthetic aperture radar (SAR) data. NSB, North Sulawesi block; MAB, Manado block; ESB, East Sulawesi block; MKB, Makassar block; NST, North Sulawesi trench; PF, Palu-Koro fault; CS, Celebes Sea. The color version of this figure is available only in the electronic edition.

during large earthquakes can help provide insight into the mechanisms of the extension of ECS.

On 29 May 2017 (UTC 14:35:21), an $M_w 6.6$ earthquake struck the central part of Sulawesi, eastern Indonesia. The epicenter, as reported by the Global Centroid Moment Tensor (CMT) catalog (see Data and Resources), was located at 1.24° S

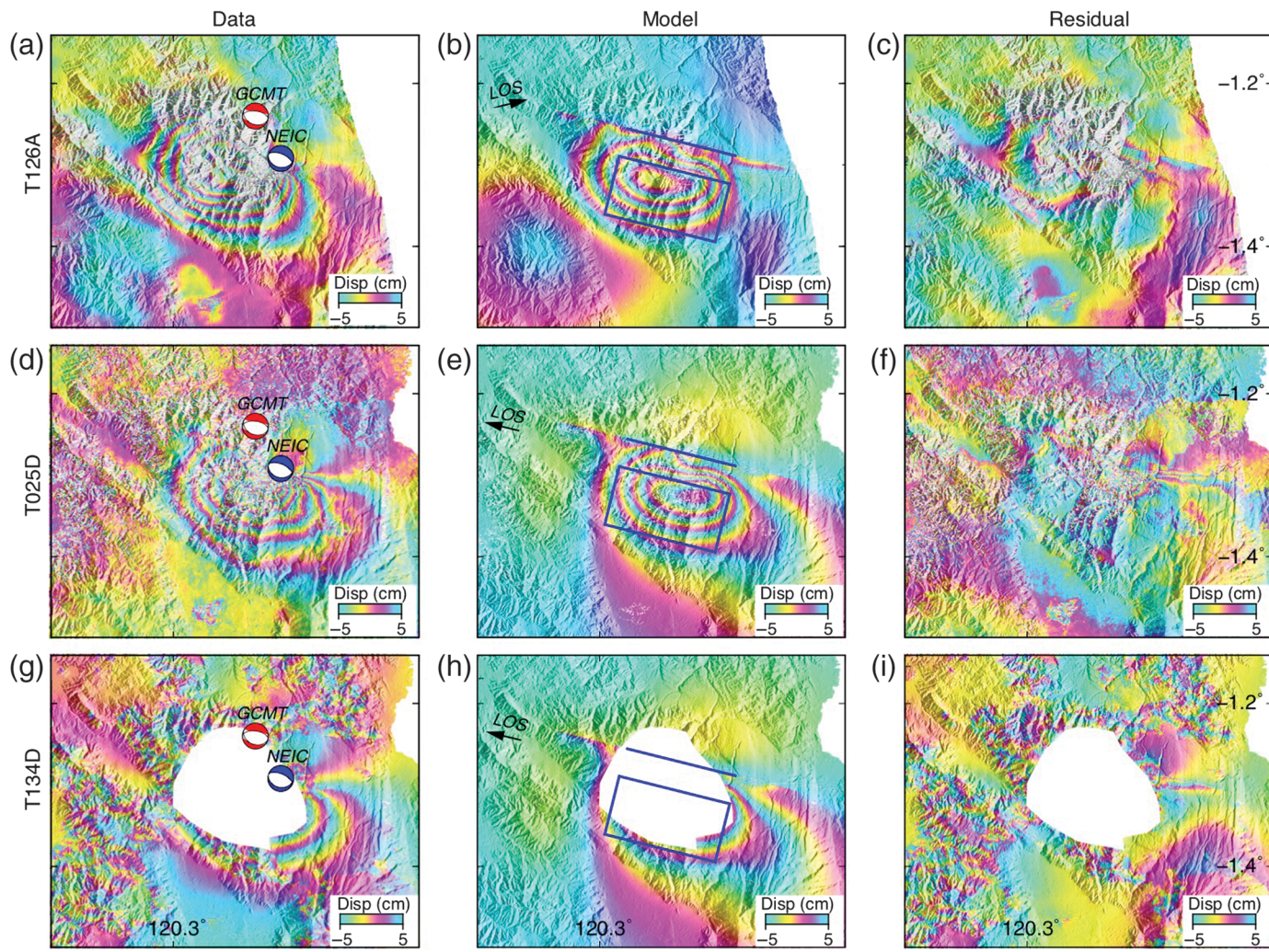
and 120.40° E approximately 39 km west-northwest of the town of Poso. The 2017 Poso earthquake, which represents the largest shallow event that has struck central Sulawesi since the implementation of modern seismic instruments, ruptured a mountainous region with a high mean elevation of ~2300 m (Fig. 1b), indicating the presence of a high-gravitational potential energy and the preferential occurrence of lithospheric extension (Dewey, 1988; Ge *et al.*, 2015).

In this article, we use coseismic ground deformation data derived from synthetic aperture radar (SAR) satellite sensors to constrain the fault geometry and invert for the slip distribution of the 2017 Poso earthquake. Based on the inverted finite slip model, we analyze the background seismicity, regional topography, and fault kinematics to obtain insights into the mechanisms of extension throughout ECS and the associated structural evolution processes.

INSAR DATA

We utilize ascending- and descending-orbit data from the Advanced Land Observing Satellite-2 (ALOS-2) and Sentinel-1 satellites (Table 1) to map the surface deformation attributable to the 2017 Poso earthquake (see Data and Resources). The ascending (T126A) and descending (T025D) data of ALOS-2 were acquired in Stripmap mode and ScanSAR mode, respectively, and the Sentinel-1 descending (T134D) data were acquired in the terrain observation with progressive scan (TOPS) imaging mode (hereafter, IM). Each interferogram in this study is processed from single-look complex products. The Gamma software is employed to process all of the data, including the alignment of single-look complex images and the subsequent interferogram generation, filtering, and unwrapping processes. The detailed SAR data processing procedure is described in the supporting information (E Text S1, available in the electronic supplement to this article). Taken that the postearthquake images were observed 2–39 days after the earthquake (Table 1), eight Sentinel-1 SAR images, spanning from 1 June to 4 September 2017, are further analyzed to evaluate the early post-seismic displacement transients and their impacts on the derived coseismic displacement (E Text S1).

Although the source region is covered by a dense rainforest with thick vegetation, the L-band ALOS-2 interferograms (shown in Fig. 2a,d) can still maintain excellent coherence, and dense fringes around the seismogenic fault are generated from both the ascending-track and the descending-track data.



▲ Figure 2. Coseismic line-of-sight (LoS) displacement of the 2017 Poso earthquake. (a) Observed LoS displacement from the ascending Advanced Land Observing Satellite-2 (ALOS-2) satellite track 126 (stripmap mode), (b) model prediction, (c) residual between (a) and (b). All results are rewrapped in the range of -5 to 5 cm. The fault plane determined through uniform slip modeling is shown in the blue rectangle, and its up-dip projection at the surface is shown by the blue line. (d–f) Same as (a–c), but for the descending ALOS-2 satellite track 25 (ScanSAR mode). (g–i) Same as (a–c), but for the descending Sentinel-1 satellite track 134. The color version of this figure is available only in the electronic edition.

The ascending- and descending-orbit ALOS-2 interferograms share the comparable deformation magnitudes and produce fringe patterns consistent with major motion away from the satellite, reflect that vertical displacement is dominated by the

subsidence (Fig. S1), and thereby suggest possible normal faulting during the Poso earthquake. The continuous northwest-southeast-oriented elliptical spatial pattern may suggest that the 2017 Poso earthquake did not break the Earth's surface

Table 1
Synthetic Aperture Radar (SAR) Data Used in This Study

Satellite	Mode	Track	Master Date (yyyy/mm/dd)	Slave Date (yyyy/mm/dd)	Perp. B (m)	σ^* (cm)	λ^\dagger (km)
ALOS-2	Strip	T126A	2017/02/03	2017/07/07	-89	2.33	5.4
	ScanSAR	T025D	2017/05/11	2017/06/22	-143	1.77	3.3
Sentinel-1	IM	T134D	2017/05/19	2017/05/31	-88	2.83	3.3

Perp. B, Perpendicular Baseline; ALOS, Advanced Land Observing Satellite.

* σ is the standard deviation (1σ) estimated from the pixels far from the deformation region.

$\dagger\lambda$ is the e-folding correlation-length scale of the experimental semivariogram.

with major slip on a buried fault. Furthermore, despite its serious decoherence in the near field, the C-band Sentinel-1 data can still provide us with some information regarding relatively far-field deformation signals (Fig. 2g). Our postseismic analysis shows that the early cumulative postseismic displacement (2–39 days after the mainshock) is minor and can be neglected (Fig. S3), suggesting that the interferograms shown in Figure 2 can well represent the coseismic deformation signals. However, the postseismic line-of-sight (LoS) displacement generated from the C-band Sentinel-1 data has a relatively low signal-to-noise ratio due to the effects of the dense vegetation in the region. More observations are still required to further clarify the possibility of the potential post-seismic slip.

SOURCE MODELING

Coseismic displacement fields derived from Interferometric Synthetic Aperture Radar (InSAR) data represent the kinematic responses of the Earth's surface to finite fault dislocations at depth. Such internal finite dislocations can be quantitatively analyzed through the dislocation geometry and magnitude, which are often called source parameters. To reconstruct the source parameters of the 2017 Poso earthquake, we follow a two-step procedure: uniform slip modeling is first performed to determine the fault geometry, and then distributed slip modeling is conducted to image the detailed slip distribution. The open-source geodetic Bayesian inversion software developed at Leeds University ([Bagnardi and Hooper, 2018](#)) is employed to perform the uniform slip modeling to obtain the best-fitting fault-geometry parameters. The Markov chain Monte Carlo and Metropolis–Hastings algorithms are subsequently employed to find the posterior probability distributions of relevant parameters. Green's functions are calculated using the elastic half-space homogeneous dislocation model ([Okada, 1985](#)) while assuming a Poisson ratio of 0.25. During the inversion, uncertainties in the SAR measurements are estimated from the experimental semivariogram ([Webster and Oliver, 2007](#)).

Table 2 and Fig. S4 show the estimated source parameters and associated confidence intervals. Our preferred uniform slip model exhibits a strike of 104° and a dip of 44° , with a length of 16 km and a width of 11 km. The uniform slip has a magnitude of 1.2 m that does not reach the Earth's surface, because the top edge of the uniform fault plane is buried at a depth of ~ 4 km. The optimal rake angle is estimated to be -95° , suggesting predominantly normal faulting during the Poso earthquake, along with some dextral slip component. Moreover, our optimal dip angle is fairly steep relative to the Global CMT and U.S. Geological Survey (USGS) solutions (Table 2).

After fixing the optimal strike, dip, and location of the source plane determined from our uniform slip modeling (Table 2), we then invert for the detailed slip through distributed slip modeling. The fault plane is enlarged to be 39 km long and 30 km wide to avoid edge effects and then parameterized by 1170 discrete, rectangular subpatches with dimensions

Table 2
Source Parameters of the 2017 Poso Earthquake

Source Parameters of the 2017 Peso Earthquake						
Model	Longitude (°)	Latitude (°)	Strike (°)	Dip (°)	Rake (°)	Length (km)
						Width (km)
USGS	120.431	-1.292	100	30	-101	-
Global CMT	120.40	-1.24	111	34	-78	-
InSAR*	120.391 ^{+0.0044} _{-0.0036}	-1.306 ^{+0.0025} _{-0.0017}	103.965 ^{+3.5146} _{-2.3835}	44.071 ^{+0.602} _{-0.4077}	-95.007 ^{+6.723} _{-4.28}	15.461 ^{+0.7763} _{-0.5124}
InSAR†	120.391	-1.306	104	44	-	39

USGS, U.S. Geological Survey; Global CMT, Global Centroid Moment Tensor; InSAR, Interferometric Synthetic Aperture Radar.

*The parameters of the uniform slip model. Longitude and latitude are the coordinates of the top center of the fault plane with the buried depth denoted by "Top". Superscripts and subscripts attached to each parameter are the 95% confidence intervals.

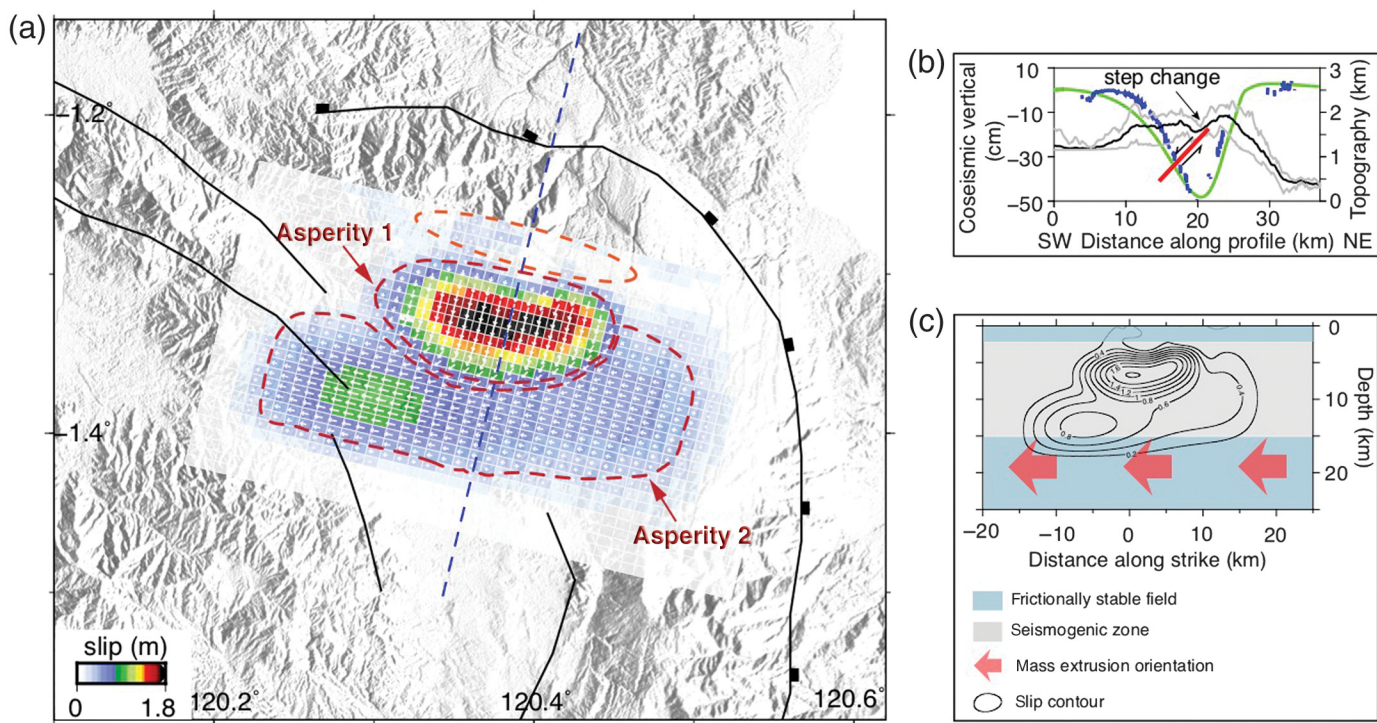
†The parameters of the distributed slip model.

USSGS, U.S. Geological Survey; Global **CVT**: Global Centroid Moment Tensor; **InSAR**: Interferometric Synthetic Aperture Radar.

*The parameters of the uniform slip model. Longitude and latitude are the coordinates of the top center of the fault plane with the buried depth denoted by "Top".

Superscripts and subscripts attached to each parameter are the 95% confidence intervals.

The parameters of the distributed slip model.



▲ Figure 3. (a) Finite slip distribution of the 2017 Poso earthquake for a fault plane that is 39 km long and 30 km wide with a strike of 104° and a dip of 44° to the south-southwest. White arrows denote the slip direction of each subpatch. The orange dashed ellipsoid depicts the zone with little or no slip in the shallow parts of the fault plane. Two significant asperities are marked by crimson dashed ellipsoids. (b) The decomposed (blue dots) and predicted (green dots) vertical deformation along the profile marked by a dotted blue line (a) together with the topography within 6 km of the profile: the averaged topography is plotted with a black curve, and the maximum and minimum topography are plotted with gray curves. The red line marks the location of the fault plane. (c) Slip contours of the main rupture and projected onto a strike-depth plane. Red arrows show the orientation of mass migration. Depth-dependent frictional properties on the fault plane are also indicated. The color version of this figure is available only in the electronic edition.

of 1 km × 1 km. Without fixing the rake angle during the modeling, the normal and strike-slip components are solved for each subpatch using the bounded-variable least-squares method (Stark and Parker, 1995); in this case, only the normal slip is allowed for the dip-slip component, whereas the strike-slip component can move freely. To avoid abrupt nonphysical variations in the slip estimation, an improved Laplacian constraint (Wang *et al.*, 2017) is applied in the inversion. The smoothing factor that balances the variables between the weighted misfit data and slip roughness is determined from the trade-off curve (Fig. S5). In addition, model solutions from 100 noise-perturbed datasets are used to evaluate the uncertainties in the coseismic distributed slip by using a Monte Carlo bootstrap-simulation technique (Parsons *et al.*, 2006).

Figure 3a shows the best-fitting distributed slip model, which clearly identifies two asperities connected along the down-dip direction. The first asperity is located at depths of 3–10 km and manifests predominantly as a normal fault with a peak slip of 1.8 m. However, the second asperity requires continued slip in down-dip zones of the first asperity and manifests predominantly as pure dextral strike slip with a peak slip of ~0.9 m. Checkerboard test (Text S2) and slip uncertainty analyses demonstrate that this deep asperity is a robust slip

feature that can be retrieved from the data (Figs. S6 and S7). Furthermore, limited slip is found in the up-dip region of the first asperity suggests that the coseismic rupture of the Poso earthquake did not propagate to or rupture the ground surface. The Poso earthquake contributes to the northeast–southwest extensional strain state and therefore the crustal thinning of ECS to some extent, due to the downward motion caused by the main rupture (Fig. 3b). The distributed-slip model yields a geodetic seismic moment of 1.16×10^{19} N · m that corresponds to an M_w 6.65 earthquake, assuming a shear modulus of 30 GPa. The static stress drop released by this earthquake is estimated to be 1.41 ± 0.2 MPa by using the law of $\Delta\sigma = CM_0/A^{3/2}$ (Kanamori and Anderson, 1975), in which A is the area of the rupture, M_0 is the seismic moment, and C is chosen to be 2.53 for rectangular cracks with an aspect ratio of 1. The predicted displacements from the best-fitting slip model fit the observations well. The root-mean-square misfits of the best-fitting model are 5.1, 3.8, and 4.8 cm for ALOS-2 ascending and descending data and Sentinel-1 descending data, respectively, all of which are within the range of an admissible error of 3σ (Table 1). The residuals can be partially explained by atmospheric artifacts in consideration of the tropical rainforest climate and possibly by early postseismic deformation.

DISCUSSION

Implications for Extrusion Tectonics in Central Sulawesi

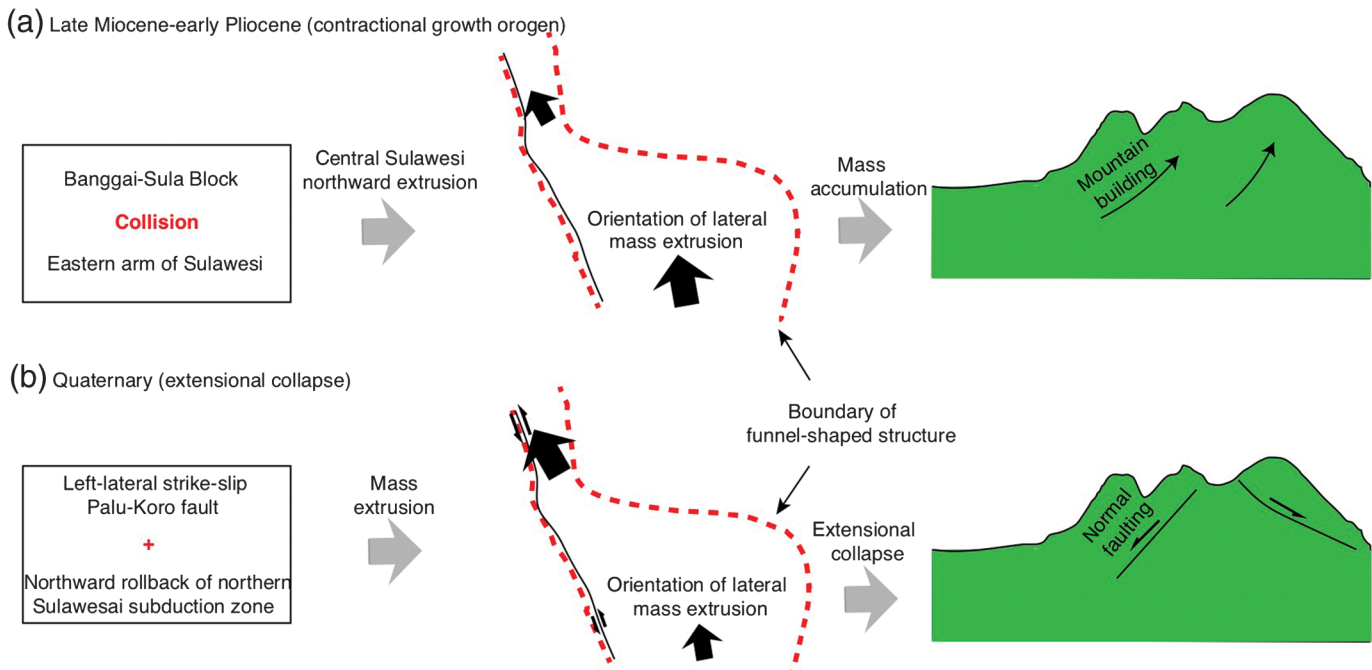
Understandably, extensional tectonic settings readily provide an environment for the formation of normal faults, whereas some normal faults preferentially occur in mountainous regions usually characterized by strike-slip tectonism. For example, the 2008 M_w 7.1 Yutian earthquake occurred on a north–south-oriented normal fault (e.g., Elliott *et al.*, 2010) 50 km south of the active Altyn Tagh fault that is dominated by a left-lateral slip rate of 9.4–11.5 mm/yr (e.g., Daout *et al.*, 2018). In addition to the northern TP, there are a large number of seismically active north–south-oriented normal faults formed across the TP during the tectonic movement of large-scale strike-slip faults in the interior of the TP (e.g., Elliott *et al.*, 2010; Ji *et al.*, 2017). The frequent seismicity throughout the TP apparently indicates an ongoing mass transportation processes involving mass accumulation and extrusion in which the transformation of gravitational potential energy plays an important role (Elliott *et al.*, 2010; Ge *et al.*, 2015), and thus this transformation has been proposed as a responsible mechanism for the lateral extrusion of the TP (e.g., Molnar and Tapponnier, 1978). Its reasonability in interpreting the regional tectonics has been evaluated in terms of the rupture of normal-faulting events in the TP (e.g., Elliott *et al.*, 2010).

As shown in Figure 1b, the major fault systems and associated high topography that outline the first-order tectonic features of ECS delineate an upside-down funnel-shaped structure (hereafter, FSS). Seismicity in this FSS is more active than in its surroundings areas (Fig. 1b), which is consistent with the GPS measurements showing that the crust of the FSS absorbs most of the elastic strain in central Sulawesi (Socquet *et al.*, 2006). The FSS is bounded by the active Palu-Koro fault and metamorphic Tokorondo complex at its western and eastern boundaries, respectively. Along the western boundary, the Palu-Koro fault cuts through the whole study region from the southeast to the northwest and accommodates 39 mm/yr of left-lateral strike-slip motion (Socquet *et al.*, 2006). Therefore, because large-scale strike-slip faults are commonly considered related to mass lateral transformation processes (e.g., Molnar and Tapponnier, 1975; Tapponnier *et al.*, 1982), the active Palu-Koro fault likely dominates the mass transformation of ECS. What's more, geological investigations show that Quaternary deformation is broadly distributed along the northern segment of Palu-Koro fault but is relatively narrow and localized along the southern segment (Bellier *et al.*, 2001). The lateral extrusion along the northern segment of the Palu-Koro fault (i.e., the outlet of the FSS) appears to be more active than its southern part (i.e., the inlet of the FSS), which is also confirmed by the dense seismic activity that is observed at the former (Fig. 1b). The eastern boundary of the FSS displays a contrasting topography that drops from ~2300 m in the west to ~500 m in the east over a lateral distance of 10 km (Fig. 3b), suggesting a high probability that this region experienced massive orogenesis in the past. The expected large gravitational potential energy could make the eastern boundary to be

a hotspot for crustal extension. Although the TP and our study region differ significantly with regard to their spatial scales, the extension in ECS likely appears to be related to a similar kinematic process, that is, gravitational collapse, considering their similar tectonic regime settings (Sulawesi and TP are both encompassed by lithospheric convergence and extension). Therefore, the existing kinematic models of the TP may lend support to an interpretation of the extensional mechanism in ECS, and vice versa.

To understand the tectonic movements and evolution of ECS, a kinematic model (Fig. 4) is proposed based on multiple sources of data, including the regional seismicity, fault kinematics, and topography. Two phases are involved in the model: mass accumulation and mass divergence (Fig. 4). In the first phase, the Banggai–Sula block collided with the eastern arm of Sulawesi in the late Miocene–early Pliocene (Bellier *et al.*, 2006), resulting in the northward motion of ECS accompanied by northward mass migration (Bellier *et al.*, 2006). Considering the local mass balance (Dewey, 1988) and the fact that the cross-sectional area of the inlet is broader than that of the outlet, this northward mass migration contributed to mass accumulation within the FSS, especially along its boundaries, where orogenesis was occurring. The second phase began during the Quaternary and has extended through the present day, and it is thought to have a close relationship to the formation of the North Sulawesi trench (NST; Bellier *et al.*, 2006), along which the floor of the Celebes Sea is subducting beneath the island of Sulawesi (Fig. 1a). In this phase, the Palu-Koro fault facilitated mass divergence toward the north, including mass injection through the southern inlet and mass extrusion through the northern outlet. This northward mass extrusion likely dominated the mass transformation process due to the greater activity of the northern segment of the Palu-Koro fault (Bellier *et al.*, 2001; Socquet *et al.*, 2006), resulting in a mass deficit at the tail end of the northern segment. As a result, mountains began to experience extensional collapse to achieve mass balance through isostatic adjustment (Dewey, 1988). Such a long-term process is believed to produce large internal deformation within the ECS and thereby accumulate substantial strain energy that will be eventually released by earthquakes in the way of normal faulting.

Sulawesi and the TP are both encompassed by lithospheric convergence and extension, which are accommodated by a mixture of active strike-slip and normal faults (e.g., Elliott *et al.*, 2010). The Palu-Koro fault in Sulawesi is believed to serve as a transform fault that kinematically links the NST to the extensional central Sulawesi (Bellier *et al.*, 2001; Socquet *et al.*, 2006). The role played by the Palu-Koro fault in the regional tectonics is similar to that played by the Red River fault in the northwestern Yunnan rift zone. The middle-southern segment of the Red River fault has been more active than its northern segment in the Quaternary (Guo *et al.*, 1996); this discrepancy definitely results in a mass deficit at the northwestern tip of the fault, thereby forming the Yunnan rift zone (e.g., Allen *et al.*, 1984; Guo *et al.*, 1996). In addition to contributing to extensional collapse, the active Palu-Koro fault, acting as the main



▲ Figure 4. Tectonic-evolution model of the funnel-shaped structure (FSS). (a) The contractional growth (i.e., orogenic) process in the late Miocene–early Pliocene, during which the mountain continued to rise, due to an increasing mass accumulation along the boundaries of the FSS. (b) The extensional collapse process during the Quaternary, during which an enormous mass was extruded from the FSS along the Palu-Koro fault. The extensional collapse of the orogen achieved mass balance and resulted in normal faulting. The color version of this figure is available only in the electronic edition.

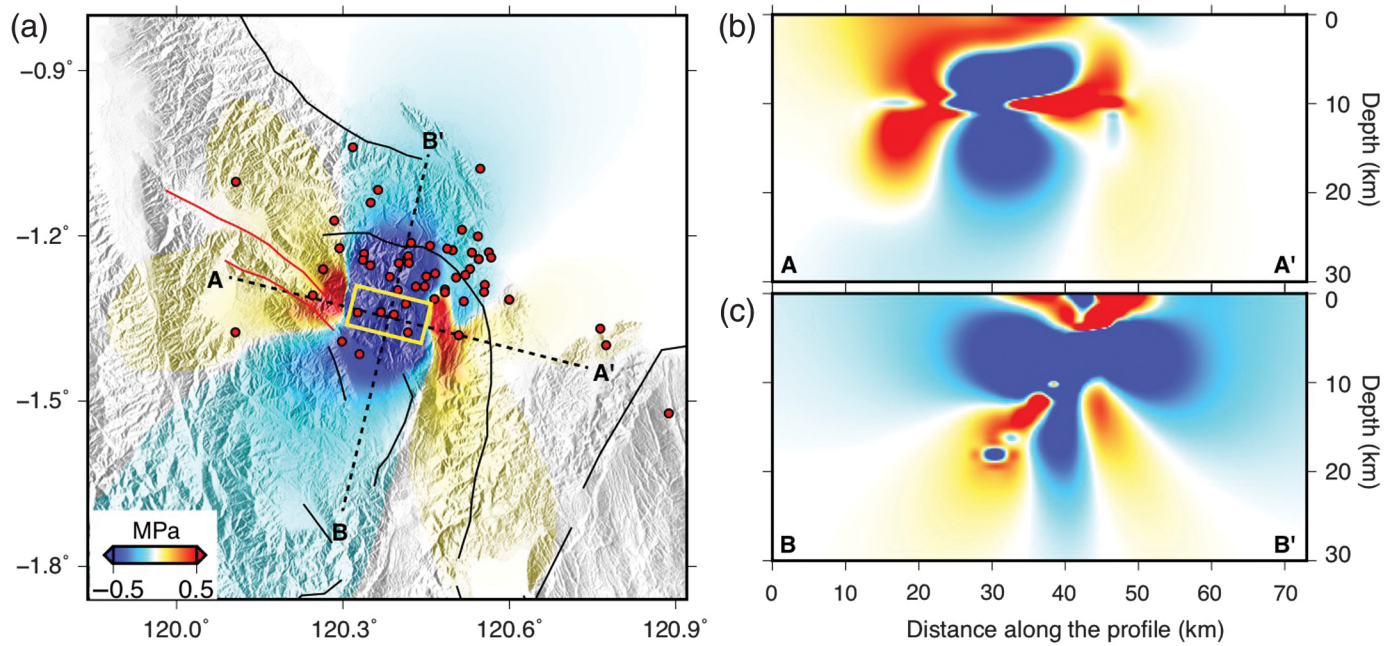
boundary of the crustal microblocks, may also dominate the motion and deformation of tectonic blocks in ECS. As Sarsito *et al.* (2017) noted, the northern part of the ECS rotates much faster (at a rate of 120 mm/My) than its southern part (at a rate of 2.5 mm/My), and this is consistent with the segmentation kinematics of the Palu-Koro fault. Alternatively, although we cannot rule out the possibility that the northward rollback of the slab beneath the NST also affects the tectonism of ECS (e.g., Bellier *et al.*, 2006), we believe that the role of this slab is minor compared with that of the active Palu-Koro fault in the regional regime, due to the great distance between ECS and NST and the limited slip rate of NST (Socquet *et al.*, 2006).

The kinematic model proposed above is supported by our preferred geodetic slip model in the sense that the kinematical characteristics of the proposed model are consistent with focal mechanisms of normal or right-lateral faulting; the distinct down-dip right-lateral faulting (the second asperity) reflects the channel of mass northward extrusion (Fig. 3c); the up-dip normal faulting (the first asperity) correspondingly reflects well the gravitational collapse of lithosphere that developed from the down-dip mass deficit, due to the northward migration of mass along the extrusion channel (Fig. 3c). One of the striking features of the slip distribution is that the depth extent of the second asperity is resolved at 10–18 km (Fig. 3c). These deep-seated, almost pure strike-slip patches coincide with a transition zone at 15–25 km that is often characterized by high-thermal gradients (Scholz, 1998). It is possible that the

ductile deformation and mass extrusion are promoted under this thermal state. The increasing tendency of mass extrusion can, on the one hand, enhance the shear stress at depth, increasing the possibility of strike-slip failure and on the other hand bring out mass deficit, leading to the development of gravitational collapse. The above investigations highlight that the proposed kinematic model is fundamentally supported by our geodetic inversion results, although we do not think it can be confirmed using this event alone. However, we should admit that this is a preliminary model that is responsible for the mechanism of extension in ECS. More constraints from geological, geophysical, and geodetic data are required to provide detailed insights into the extension in central Sulawesi. Our kinematic model may have some implications for the 2018 M_w 7.5 Palu earthquake that ruptured the northern Palu-Koro fault (Fig. 1b). The 2018 M_w 7.5 earthquake is predominated by left-lateral strike slip and could show an early and persistent supershear rupture speed (Bao *et al.*, 2018).

Implications for Potential Hazards

The Poso earthquake contributes to the northeast–southwest extension in central Sulawesi that is in agreement with the strain state revealed by GPS measurements (e.g., Sarsito *et al.*, 2017). However, because strong normal earthquakes ($M_w > 6$) are absent in ECS since the instrumental records, the 2017 Poso earthquake may mark a critical point in time after which such earthquakes will occur with greater frequency throughout the study region. To assess the impact of the Poso earthquake on



▲ Figure 5. The Coulomb failure stress (CFS) change at (a) a depth of 7 km and (b) along the profiles A–A' and (c) B–B'. The two black dashed lines mark the surface trace of the CFS profiles in Figure 5b,c. Black lines are regional faults. Red dots represent the aftershocks recorded by the ISC. The yellow rectangle is the fault plane of the uniform model. The color version of this figure is available only in the electronic edition.

the regional seismic risk, we calculate the Coulomb failure stress (CFS) changes (e.g., Lin and Stein, 2004; Toda *et al.*, 2005) at a depth of 7 km (where the maximum slip occurs), based on our best-fitting distributed slip model that assumes a friction coefficient of 0.4, with a receiver fault consisting of a strike of 104° , dip of 44° , and rake of -95° . Figure 5a shows that the CFS along two faults located to the west of the main rupture were increased by ~ 0.1 MPa, which greatly enhances the potential seismic risk if these two faults are prestressed and near the critical taper. This is further validated by the CFS calculated on the regional faults around the epicentral area, in which the variable orientations were considered (Fig. S8). In addition, no significant slip was observed at shallow depths of 0–3 km; this is possibly related to the presence of a metamorphic complex in the shallow crust (Spencer, 2010, 2011), because layers of weaker lithology could manifest through velocity-strengthening friction (Scholz, 1998). A geometry variation at the shallow depths may form a structural barrier with strong frictional resistance and could also prevent the event from rupturing to the surface. Therefore, although the CFS was also increased at shallow depths of 0–3 km (Fig. 5b,c), we speculate that the potential seismic risk remains low, due to the velocity-strengthening friction of the metamorphic complex or the high-critical stress on faults, whereas the possibility of aseismic creep cannot be ruled out. However, it remains a challenge to investigate the trigger mechanisms of aftershocks, due to the lack of relocated aftershock sequences, which requires further study. What's more, the occurrence of the 2018 M_w 7.5 Palu earthquake could be hard-related to the static CFS triggered by the 2017 Poso earthquake (Fig. 5).

CONCLUSION

Source parameters of the 2017 Poso earthquake are investigated using the InSAR data. Results show that the earthquake ruptured along a moderate dip plane of 44° ; the main rupture was dominated by a normal-faulting mechanism at a depth of 3–10 km; some distinct dextral strike slip are also identified along the down-dip zones of normal faulting. The coseismic rupture supports the kinematic model proposed for the explanation of regional tectonics in central Sulawesi. The model highlights that extension in regional central Sulawesi is primarily driven by gravitational collapse, in which mass lateral extrusion along the Palu-Koro fault played an important role.

DATA AND RESOURCES

The Advanced Land Observing Satellite-2 (ALOS-2) PALSAR-2 synthetic aperture radar (SAR) data are provided by the Japan Aerospace Exploration Agency (JAXA) through the RA6 project (ID: 3048). The Sentinel-1 SAR data are provided by the European Space Agency (ESA) through the Copernicus Open Access Hub (<https://vertex.daac.asf.alaska.edu/>, last accessed June 2017). The moment tensor solution is from the U.S. Geological Survey (USGS; <http://earthquake.usgs.gov>, last accessed June 2017) and the Global Centroid Moment Tensor project (CMT; <http://www.globalcmt.org>, last accessed June 2017). The aftershock locations are from the International Seismological Centre (ISC; <http://www.isc.ac.uk>, last accessed August 2017). The slip model inferred in this study is available at the following

link (<https://github.com/shuawang123/PosoSlipModel.git>, last accessed December 2018). 

ACKNOWLEDGMENTS

The authors thank Associate Editor Brendan Crowell and Editor-in-Chief Zhigang Peng for their insightful comments that helped us to improve the article and also thank anonymous reviewers. This work is supported by the National Natural Science Foundation of China under Grant Numbers 41431069 and 41774011, by the Hong Kong Polytechnic University Start-up Grant (1-ZE6R) and by the Hong Kong Research Grants Council Early Career Scheme Fund (Project Number F-PP4B). Most figures are plotted using the Generic Mapping Tools ([Wessel et al., 2013](#)).

REFERENCES

- Allen, C. R., A. R. Gillespie, H. Yuan, K. E. Sieh, Z. Buchun, and Z. Chengnan (1984). Red River and associated faults, Yunnan Province, China: Quaternary geology, slip rates, and seismic hazard, *Geol. Soc. Am. Bull.* **95**, no. 6, 686–700.
- Bagnardi, M., and A. Hooper (2018). Inversion of surface deformation data for rapid estimates of source parameters and uncertainties: A Bayesian approach, *Geochem. Geophys. Geosys.* **19**, doi: [10.1029/2018GC007585](https://doi.org/10.1029/2018GC007585).
- Bao, H., J. P. Ampuero, L. Meng, E. J. Fielding, C. Liang, H. Huang, and T. Feng (2018). Early and persistent supershear rupture of the 2018 M_w 7.5 Palu earthquake, doi: [10.31223/osf.io/tuasf](https://doi.org/10.31223/osf.io/tuasf).
- Bellier, O., M. Sébrier, T. Beaudouin, M. Villeneuve, R. Braucher, D. Bourlès, L. Siame, E. Putranto, and I. Pratomo (2001). High slip rate for a low seismicity along the Palu-Koro active fault in central Sulawesi (Indonesia), *Terra Nova* **13**, no. 6, 463–470.
- Bellier, O., M. Sébrier, D. Seward, T. Beaudouin, M. Villeneuve, and E. Putranto (2006). Fission track and fault kinematics analyses for new insight into the Late Cenozoic tectonic regime changes in West-Central Sulawesi (Indonesia), *Tectonophysics* **413**, nos. 3/4, 201–220.
- Copley, A., J.-P. Avouac, and B. P. Wernicke (2011). Evidence for mechanical coupling and strong Indian lower crust beneath southern Tibet, *Nature* **472**, no. 7341, 79–81.
- Cummins, P. R., and I. Meilano (2017). Geohazards in Indonesia: Earth science for disaster risk reduction, *Geol. Soc. Lond. Spec. Publ.* **441**, no. 1, SP441.11, 135 pp.
- Daout, S., M.-P. Doin, G. Peltzer, C. Lasserre, A. Socquet, M. Volat, and H. Sudhaus (2018). Strain partitioning and present-day fault kinematics in NW Tibet from Envisat SAR interferometry, *J. Geophys. Res.* **123**, no. 3, 2462–2483.
- Dewey, J. F. (1988). Extensional collapse of orogens, *Tectonics* **7**, no. 6, 1123–1139.
- Elliott, J. R., R. J. Walters, P. C. England, J. A. Jackson, Z. Li, and B. Parsons (2010). Extension on the Tibetan plateau: Recent normal faulting measured by InSAR and body wave seismology, *Geophys. J. Int.* **183**, no. 2, 503–535.
- Ge, W.-P., P. Molnar, Z.-K. Shen, and Q. Li (2015). Present-day crustal thinning in the southern and northern Tibetan Plateau revealed by GPS measurements, *Geophys. Res. Lett.* **42**, 5227–5235, doi: [10.1002/2015GL064347](https://doi.org/10.1002/2015GL064347).
- Guo, S., H. Xiang, F. Ji, and W. Zhang (1996). A study on the relation between quaternary right-lateral slip and tip extension along the Honghe fault, *Seismol. Geol.* **18**, no. 4, 301–309 (in Chinese).
- Hall, R., and W. Spakman (2015). Mantle structure and tectonic history of SE Asia, *Tectonophysics* **658**, 14–45.
- Hamilton, W. (1979). Tectonics of the Indonesian region, *U.S. Geol. Surv. Profess. Pap.* **1078**, 345 pp. + map.
- Ji, L., Q. Wang, J. Xu, and J. Feng (2017). The 1996 M_w 6.6 Lijiang earthquake: Application of JERS-1 SAR interferometry on a typical normal-faulting event in the northwestern Yunnan rift zone, SW China, *J. Asian Earth Sci.* **146**, 221–232.
- Kanamori, H., and D. L. Anderson (1975). Theoretical basis of some empirical relations in seismology, *Bull. Seismol. Soc. Am.* **65**, no. 5, 1073–1095.
- Lin, J., and R. S. Stein (2004). Stress triggering in thrust and subduction earthquakes, and stress interaction between the southern San Andreas and nearby thrust and strike-slip faults, *J. Geophys. Res.* **109**, no. B02303, doi: [10.1029/2003JB002607](https://doi.org/10.1029/2003JB002607).
- Molnar, P., and P. Tapponnier (1975). Cenozoic tectonics of Asia: Effects of a continental collision, *Science* **189**, no. 4201, 419–426.
- Molnar, P., and P. Tapponnier (1978). Active tectonics of Tibet, *J. Geophys. Res.* **83**, 5361–5376.
- Okada, Y. (1985). Surface deformation due to shear and tensile faults in a half-space, *Bull. Seismol. Soc. Am.* **75**, no. 4, 1135–1154.
- Parsons, B., T. Wright, P. Rowe, J. Andrews, J. Jackson, R. Walker, M. Khatib, M. Talebian, E. Bergman, and E. R. Engdahl (2006). The 1994 Sefidabeh (eastern Iran) earthquakes revisited: New evidence from satellite radar interferometry and carbonate dating about the growth of an active fold above a blind thrust fault, *Geophys. J. Int.* **164**, no. 1, 202–217.
- Sarsito, D. A., Susilo, W. J. F. Simons, H. Z. Abidin, B. Sapiie, W. Triyoso, and H. Andreas (2017). Rotation and strain rate of Sulawesi from geometrical velocity field, *AIP Conference Proceedings*, Vol. 1857, no. 1, 040006, AIP Publishing.
- Scholz, C. H. (1998). Earthquakes and friction laws, *Nature* **391**, no. 6662, 37.
- Silver, E. A., R. McCaffrey, and R. B. Smith (1983). Collision, rotation, and the initiation of subduction in the evolution of Sulawesi, Indonesia, *J. Geophys. Res.* **88**, 9407–9418.
- Socquet, A., W. Simons, C. Vigny, R. McCaffrey, C. Subarya, D. Sarsito, B. Ambrosius, and W. Spakman (2006). Microblock rotations and fault coupling in SE Asia triple junction (Sulawesi, Indonesia) from GPS and earthquake slip vector data, *J. Geophys. Res.* **111**, no. B08409, doi: [10.1029/2005JB003963](https://doi.org/10.1029/2005JB003963).
- Spencer, J. E. (2010). Structural analysis of three extensional detachment faults with data from the 2000 Space-Shuttle Radar Topography Mission, *GSA Today* **26**, no. 8, 4–10.
- Spencer, J. E. (2011). Gently dipping normal faults identified with Space Shuttle radar topography data in central Sulawesi, Indonesia, and some implications for fault mechanics, *Earth Planet. Sci. Lett.* **308**, nos. 3/4, 267–276.
- Stark, P. B., and R. L. Parker (1995). Bounded-variable least-squares: An algorithm and applications, *Comput. Stat.* **10**, 129–129.
- Stevens, C., R. McCaffrey, Y. Bock, J. Genrich, C. Subarya, S. S. O. Puntodewo, and C. Vigny (1999). Rapid rotations about a vertical axis in a collisional setting revealed by the Palu fault, Sulawesi, Indonesia, *Geophys. Res. Lett.* **26**, no. 17, 2677–2680.
- Tapponnier, P., G. Peltzer, A. Y. Le Dain, R. Armijo, and P. Cobbold (1982). Propagating extrusion tectonics in Asia: New insights from simple experiments with plasticine, *Geology* **10**, no. 12, 611–616.
- Toda, S., R. S. Stein, K. Richards-Dinger, and S. Bozkurt (2005). Forecasting the evolution of seismicity in southern California: Animations built on earthquake stress transfer, *J. Geophys. Res.* **110**, no. B05S16, doi: [10.1029/2004JB003415](https://doi.org/10.1029/2004JB003415).
- Wang, S., C. Xu, Y. Wen, Z. Yin, G. Jiang, and L. Fang (2017). Slip model for the 25 November 2016 M_w 6.6 Aketao earthquake, Western China, revealed by Sentinel-1 and ALOS-2 observations, *Rem. Sens.* **9**, no. 4, 325.
- Webster, R., and M. A. Oliver (2007). *Geostatistics for Environmental Scientists*, Second Ed., John Wiley & Sons, Chichester, United Kingdom.

Wessel, P., W. H. Smith, R. Scharroo, J. Luis, and F. Wobbe (2013).
Generic mapping tools: Improved version released, *Eos Trans. AGU*, 94, no. 45, 409–410.

Hong Kong, China
wenbin.xu@polyu.edu.hk

Shuai Wang
Caijun Xu
Yangmao Wen
School of Geodesy and Geomatics
Wuhan University
No. 129, Luoyu Road, Hongshan District
Wuhan 430079, China
cjxu@sgg.whu.edu.cn

Zhi Yin
Institute of Geodesy
University of Stuttgart
Geschwister-Scholl-Str. 24D
70174 Stuttgart, Germany

Guoyan Jiang
Earth System Science Program
The Chinese University of Hong Kong
Shatin, NT
Hong Kong 999077, China

Wenbin Xu
Department of Land Surveying and Geo-informatics
The Hong Kong Polytechnic University
No. 181, Chatham Road South, Hung Hom, Kowloon

Published Online 27 December 2018